

Estimation and correction for GC-content bias in high throughput sequencing

Yuval Benjamini¹ and Terence P. Speed^{1,2}

¹Department of Statistics, University of California at Berkeley, Berkeley, CA 94720

²Bioinformatics Division, Walter and Eliza Hall Institute, Victoria 3050, Australia

June 24, 2011

1 Abstract

GC-content bias describes the dependence between fragment count (read coverage) and GC content found in high-throughput sequencing assays, particularly the Illumina Genome Analyzer technology. This bias can dominate the signal of interest for analyses that focus on measuring fragment abundance within a genome, such as copy number estimation. The bias is not consistent between samples, and current methods to remove it in a single sample do not assume any knowledge of the curve shape or scale. In this work we analyze regularities in the GC-bias patterns, and find a compact description for this curve family. It is the GC content of the full DNA fragment, not only the sequenced read, that most influences fragment count. This GC effect is unimodal: both GC rich fragments and AT rich fragments are under-represented in the sequencing results. Based on these findings, we propose a new method to calculate predicted coverage and correct for the bias. This parsimonious model produces single bp prediction which suffices to predict the GC effect on fragment coverage at all scales, all chromosomes and for both strands; this allows optimal GC-effect correction regardless of the downstream smoothing or binning. We demonstrate our model's potential for improving on current approaches to copy-number estimation. These GC-modeling considerations can also inform other high-throughput sequencing analyses such as ChIP-seq and RNA-seq. Finally, our analysis provides empirical evidence strengthening the hypothesis that PCR is the most important cause of the GC bias.

2 Introduction

Since it was introduced, Illumina Genome Analyzer high-throughput sequencing has become an increasingly popular technology for determining relative abundance of DNA in an assay. In this method, the DNA of interest is fragmented, and one or both ends of the fragment are sequenced. These sequenced short reads, or read-pairs, are aligned to a reference genome. Counts of aligned fragments may be used to measure DNA copy number (DNA-seq), protein binding (ChIP-Seq) or expression (in RNA-seq). In many of these assays, researchers would like to compare such

fragment-counts between different locations in the genome. It is therefore troubling that the number of reads mapped to a genomic region depends considerably on the sequence itself.

One well-documented [7] dependency is the GC-content bias, that between the proportion of G and C bases in a region and the count of fragments mapped to it. (We use *fragment count*, instead of *read count / read coverage* because paired-reads identify a fragment). This variability does not reflect the signal of interest, but might confound it: Because GC abundance is heterogeneous across the genome and often correlated with functionality, the GC effect can be hard to tell apart from the true signal. The effect does not decay even for larger bins: large differences ($> 2X$) in coverage are common even in 100 kb bins [6]. To make matters harder, the effect is not consistent between repeated experiments, or even libraries within the same experiment (see below). Estimating and directly correcting for this effect has become a well-established step in protocol design [17], quality control [13], and studies [9] [21] using high throughput sequencing.

Most current correction methods follow a common path. Both fragment counts and GC counts are binned to a bin-size of choice. A curve describing the conditional mean fragment count per GC value is estimated (by binning[21], or assuming smoothness[3][15]). The resulting GC curve determines a predicted count for each bin based on the bin's GC. These predictions can be used directly to normalize the original signal, or as the rates for a heterogeneous Poisson model. Bin size is arbitrarily set, usually to match down-stream analysis. While these methods remove most of the GC effect, they do not use any prior knowledge about the effect. This is perhaps why key features of the GC curve, such as its unimodality, have sometimes been overlooked or completely missed in the estimation.

While GC effect is commonly corrected for, until recently studies regarding the nature of this bias have been rare. Dohm (2008)[7] first described the effect of the GC on fragment coverage in Illumina GA. The effect they found seemed highly linear - fragment coverage increased with GC content, but they sequenced genomes that were GC poor. This is probably why the GC effect is sometimes described as the correlation between GC and coverage [20]. In later high-throughput studies of the human genome, plots of GC-curves usually reflect non-linear curves, but are rarely investigated further than non-parametric fitting. Identifying the source of the bias was also hard, because the composition of the DNA molecule can affect multiple stages of the protocol. Sequence related biases in the priming [8], size-selection [17], PCR [11], and probability of sequencing-errors [16] [1] [4] have all been found. In a recent analysis [1], PCR was shown to play the dominant role in the stages before the sequencing. While sequencing protocols have partially evolved to accommodate this new understanding[11], estimation and correction methods have not.

From a technical point of view, the above sources of bias cluster according to the location and length scale of GC thought to be driving the non-uniformity in the counts. Locally, GC counts could be associated with the stability of the DNA, and thus modify the probability of a fragmentation-point occurring in the genome, leading to a *fragmentation model*. The GC content could primarily modify the base-sequencing process; we call this the *read model*, suggesting that the GC of the forward read (in the single-end) or both reads (in the paired end case) best explain fragment count. *Full-fragment models* assume the GC of the whole fragment determines which fragments are selected or amplified. Finally, *global models* refer to GC effects on scales larger than the fragment length, e.g., through an association with some higher-order structure of the DNA. These loosely defined models can be realized statistically by counting the GC in a suitable region and comparing that to fragment coverage. While the differences between the above models might seem small, they are sometimes considerable (see below). Note that any GC-bias removal

strategy is implicitly choosing a GC-bias model when it uses GC in some region to correct for the effect.

In this work, we take a descriptive approach to investigating the common structures found in GC-curves in DNA-seq. We study the effect of GC on fragment count in many DNA-sequencing copy-number assays for (both normal and tumor) high-coverage human genomes, taken from multiple labs. Copy-number for normal genomes should rarely change, and so observed variability in fragment count can almost always be attributed to technical effects rather than biological signal. We use a single position model to estimate the effect of GC on the fragment counts, and seek a parsimonious description for this family of curves. (The same model underlies the correction method BEADS, see [5]). Such a description has two main advantages: it allows more accurate estimation of the GC curve by highlighting an appropriate set of parameters; and it provides important empirical evidence regarding the experimental stages that may cause or modify this effect.

The data we analyze suggests that to a large extent, the dependence between count and GC originates from a biased representation of possible DNA-fragments, with both high GC and high AT fragments being underrepresented. This global structure of the GC dependence is consistent, but the exact shape varies considerably across samples, even matched samples. We describe a parsimonious model for the GC effect, and show it suffices to predict the GC effect on fragment coverage on all scales, all chromosomes and for both strands. This prediction is better than generic fitting approaches currently used, as illustrated on DNA-seq with and without copy-number events. Our model produces single bp prediction, allowing optimal correction regardless of the required downstream smoothing. Finally, this provides empirical evidence strengthening the hypothesis that PCR is the most important cause for GC bias.

3 Materials and Methods

3.1 Mapped read files

The main data set we use consists of two samples of DNA from an ovarian cancer patient: one sample from the tumor and another normal sample (from white blood cells). Each of these DNA samples was turned into two separate fragment libraries, differing in fragment length distribution. Fragments were sequenced on both ends - 75 base-pair reads on each end - according to standard Illumina procedures. Each fragment was then mapped back to the human reference genome, based on the 5' read. These sequenced read pairs were mapped to a reference using BWA (version-0.4.9) [12]. Unless otherwise mentioned, all plots are from chromosome 1 of normal Lib1. Two additional DNA-seq data sets from other labs are shown, one tumor and one normal, see details in Table 1.

For each library, this procedure resulted in a list of fragments. Each fragment can be described by the location of its 5' end (chromosome, location and strand), and its length. Length was inferred from the mapping of the 3' end, based on the paired-end alignment of BWA. Only those pairs in which the 5' read was uniquely mapped were kept (flag XT:A:U of BWA). However, we did not discard a pair when the 3' was not mapped; thus for most of this analysis, the fragment set is similar to that obtained from single-end data. Only where fragment length is explicitly discussed did we remove fragments lacking 3' information ($\sim 1\%$ of fragments). No additional quality filtering was applied.

Name	Type	Date	Institute	Frag.	Reads (bp)
TCGA-13-0723-01A Lib1	Ovarian Tumor	Apr 2009	Wash U	173 ± 22	76
TCGA-13-0723-01A Lib2	Ovarian Tumor	Apr 2009	Wash U	293 ± 31	76
TCGA-13-0723-10B Lib1	Matched Normal	Apr 2009	Wash U	154 ± 17	76
TCGA-13-0723-10B Lib2	Matched Normal	Apr 2009	Wash U	284 ± 38	76
HCC1569	Breast Tumor	Jan 2009	UC Berkeley	507 ± 40	45
HG00262 (1000 Genomes)	Healthy	Aug 2010	Broad Inst.	375 ± 80*	75

(*) Size distribution of longest 80% fragments of HG00262 is tight, but with long left tail.

Table 1: **List of data sets analyzed in this paper.** The top pair and the second pair are each two libraries from the same genome.

3.2 Loess model

Previous analyses of GC focused on the relation between fragment count and GC composition for particular bin sizes (see for example [3],[10]). We call this the *loess model*, and describe shortly how we reproduce such estimation. For a given bin (interval of the genome), GC is the fraction of G and C bases in that bin according to the reference genome. Bin counts are the total number of (forward) fragments with 5'-end inside the bin. To account for uniqueness of sequences, a mappability measure is calculated for each position (base pair) in the bin. A location is called *mappable* if the k -mer of the reference genome starting at the location is not perfectly repeated at any another location in the genome, where k is the read length (checked by a Python script using the Bowtie mapper [18]). All subsequent analysis is done in R [19]. The GC-bias curve is determined by loess regression of count by GC (using the *loess* R package) on a random sample of 10,000 high mappability (> 0.9) bins. (We use a smoothness parameter of 0.3 in loess, and set estimated rates to 0 for GC values with few data points).

3.3 Single position models

We call *single position models* those models that estimate the *mean fragment count* (the *rate*) for individual locations rather than bins. We consider a family of such models linking fragment count to GC, where the expected count of fragments starting (5' end) at x depends on the GC count in a window that starts a bp from x . (Figure 1 illustrates the case in which GC is computed from a 4-bp window starting at the fragment 5' end). Each such model can be characterized by the shift a and the length l of its “driving” GC window. $W_{a,l}$ denotes the model in which the fragment count starting at x (5' end) depends on the GC between $x + a$ and $x + a + l$. (We will use $GC(x + a, l)$ for the GC count of the l bp window starting at $x + a$). For example, in $W_{0,r}$ the fragment count is determined by the GC of the first r bp of the fragment. The model $W_{a,l}$ has $l + 1$ rate parameters, $\lambda_0 \dots \lambda_l$, corresponding to windows with $gc = 0, \dots, l$.

The following is a description of our method of estimating the parameters for a single position model $W_{a,l}$. A large ($n \approx 10$ million) random sample of mappable locations is taken from the genome. Large genomic regions with either zero fragment-counts or with counts that are extremely high (> 0.99 quantile + median) were removed from the sample. The sample is partitioned (stratified) according to the GC of the reference genome: if $gc = GC(x + a, l)$ then position x is assigned to stratum S_{gc} . Let N_{gc} denote the number of sample positions assigned to S_{gc} . Note that the assignment to strata depends only on properties of the model and the

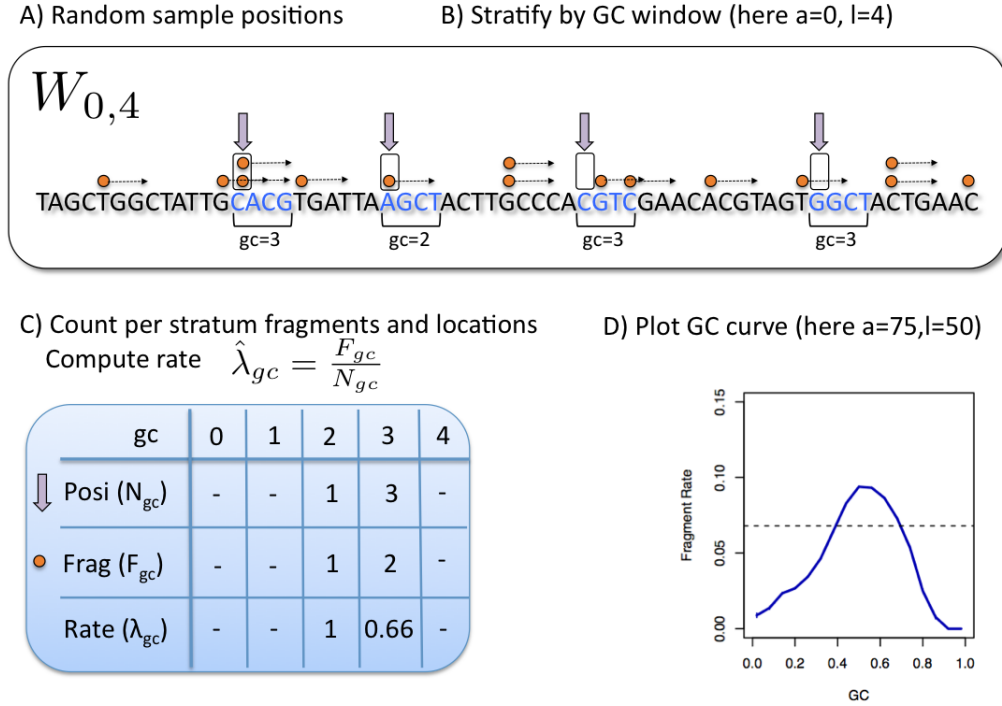


Figure 1: **Single position model estimation.** (A) Mappable positions along the genome are randomly sampled (arrows); (B) These positions are stratified by the GC count in the corresponding sliding window (here $a = 0, l = 4$); (C) The number of fragments with 5' end (circles) in sampled locations are counted; (D) Mean fragment rates for each stratum are estimated, taking the ratio between fragment count and positions in the stratum. These form the GC curve (here the curve for $a = 75, l = 50$ from Figure 4(C)).

reference genome, not on the sequencing data.

Next, for every value of gc , we count the total number F_{gc} of fragments starting (5' end) at the x 's in S_{gc} . We estimate λ_{gc} by taking the ratio

$$\hat{\lambda}_{gc} = \frac{F_{gc}}{N_{gc}}$$

The random sample is taken over (potential) **positions** in reference genome, not **fragments**. The estimated fragment rates implicitly account for the total number F of mapped fragments in the sample ($F = \sum_{gc=0}^l N_{gc} \hat{\lambda}_{gc}$). For large windows, we expect many strata to be small. Strata are then pooled together (constant jumps of 3 or 6 are used). The parameters that were skipped are then estimated by interpolation using loess regression (smoothness 0.2).

3.3.1 Comparing models

An estimated model $W_{a,l}$ (i.e. each choice of GC-window) can be used to generate predicted counts for any genomic region. Models can be compared based on the quality of their corrections (see below). However, this is very inefficient, and we consider a simpler surrogate measure that

allows comparison of many different models regardless of window size. We use the normalized *total variation distance* (TV) between the stratified estimated rates and a uniform rate (equal to the global mean rate in our sample $\hat{\lambda} = F/n$)

$$TV(W_{a,l}, U) = \frac{1}{2\hat{\lambda}} \sum_{gc=0}^l \frac{N_{gc}}{n} |\hat{\lambda}_{gc} - \hat{\lambda}|.$$

The above score (TV score) is a weighted L_1 distance from the global mean, normalized by $\frac{1}{2\hat{\lambda}}$ (so it will be between 0 and 1). In other words, it is the total variation distance between the empirical distribution for a single fragment (under specific GC categories) and a uniform distribution. Thus, it measures the proportion of fragments influenced by the stratification, and is comparable across data sets. We look for **high TV**, meaning counts are strongly dependent on GC under a particular stratification. This could indicate that correcting for such a model would **best correct** for the GC dependence.

3.3.2 Fragment length models

To measure the effect of fragment lengths, a separate single position model is fit for fragments of each length. $W_{a,l}^s$ accounts for the fragments of length s only. The locations in the sample are still partitioned according to gc , but instead of counting all fragments starting at x 's in S_{gc} , only fragments of length s are counted (F_{gc}^s). Rates are estimated as before,

$$\hat{\lambda}_{gc}^s = F_{gc}^s / N_{gc}.$$

For the fragment length model, we would like to model the count of fragments using the GC in the fragment after removing a few bp from each end. Hence, the GC-window size l becomes $s - a - m$. The model $W_{a,s-a-m}^s$ is then determined by a the shift from the fragment 5' end, and m the margin from the 3' end.¹ The parameters of this model are rates for each combination of fragment length and GC. The rate surface is smoothed using a 2D Gaussian kernel ($\theta = 0.7$ for estimation, $\theta = 1.8$ for visualization - Figure 5).

3.3.3 Predicted rates

The mean fragment count μ_x predicted for a genomic position x using $W_{a,l}$ is

$$\hat{\mu}_x = \begin{cases} \hat{\lambda}_{GC(a,x+l)} & \text{if } x \text{ is uniquely mappable} \\ 0 & \text{otherwise.} \end{cases}$$

For the fragment length model, $\{W_{a,s-a-m}^s\}_s$, the predicted count of fragments from all lengths (if x is mappable) is the sum of predictions for each length

$$\hat{\mu}_x = \begin{cases} c \cdot \sum_s \hat{\lambda}_{GC(x+a,s-m)}^s & \text{if } x \text{ is uniquely mappable} \\ 0 & \text{otherwise.} \end{cases}$$

¹Note that if l had been instead fixed for any s , the set $\{W_{a,l}^s\}$ would be a refinement of $W_{a,l}$, with $F_{gc} = \sum_s F_{gc}^s$ and $\hat{\lambda}_{gc} = \sum_s \hat{\lambda}_{gc}^s$. This is not the case here, because the GC-window grows with the fragment length.

with c a scaling to equalize predicted and observed total fragment counts (based on the fraction of fragments with unknown length). Finally, the mappability model uses the global mean ($\hat{\lambda}$) as the predictor for each mappable position

$$\hat{\mu}_x = \begin{cases} \hat{\lambda} & \text{if } x \text{ is uniquely mappable} \\ 0 & \text{otherwise.} \end{cases}$$

Fragment counts in bins are additive, so for any bin b the predictor is $\hat{\mu}_b = \sum_{x \in b} \hat{\mu}_x$. Reverse strand follows similar fragment rates when the GC window direction is reversed (see below). To show this, we estimate the strands separately except where otherwise stated.

3.4 Evaluation

We evaluate the success of a model by comparing its predictions ($\hat{\mu}$) to the vector of observed fragment counts (\mathbf{F}). For robust evaluation, we measure the mean (average) absolute deviation (MAD) between predicted and observed counts. Let B be the set of bins, and F_b the count of fragments for which 5' end is inside of bin b .

$$MAD(\mathbf{F}, \hat{\mu}) = \text{avg}_{b \in B} |F_b - \hat{\mu}_b|.$$

For visualization, observed counts are normalized by their respective predicted values, creating an implicit measure of copy number (CN). That is, we plot

$$CN_b(F_b, \hat{\mu}_b) = \frac{F_b + \epsilon}{\hat{\mu}_b + \epsilon},$$

where $\epsilon = 0.1$ to stabilize this estimate when predicted number of fragments is small. On non-tumor data, we expect these values to be concentrated around 1, and the spread should indicate the quality of the predictions.

3.4.1 Comparisons with Poisson variation

We compare the variation around the predicted means to the expected variation of a Poisson. Let \bar{F} be the mean fragment count, and F_b the fragment count in bin b as before. Then

$$\text{Total Variance} = \frac{1}{|B|} \sum_{b \in B} (F_b - \bar{F})^2$$

and for some model giving predictions $\hat{\mu}_b$,

$$\text{Residual Variance} = \frac{1}{|B|} \sum_{b \in B} (F_b - \hat{\mu}_b)^2$$

Poisson variance is taken to be \bar{F} . Only extremely high counts ($F_b > 0.99$ quantile + median(\mathbf{F})) were removed from these.

Although we remove extreme high counts, variances can be influenced by a relatively small set of bins with high counts. We would like to compare residual variation of the different models in a way that is more robust to those. Following [2], we look at the empirical quantile curves. For a given model, we grouped counts from 1 kb bins according to their predictions ($\hat{\mu}_b$'s). We

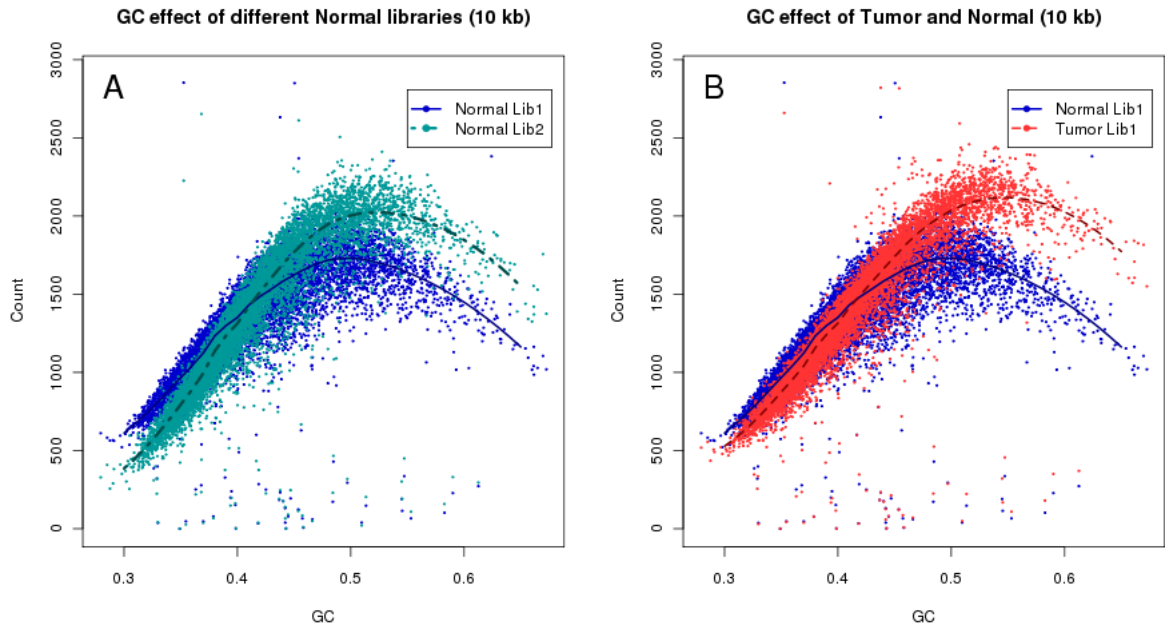


Figure 2: **GC curves (10 kb bins)**. Observed fragment counts and loess lines plotted against GC of (A) two libraries from the same normal sample, and (B) the tumor library (red) with its matched normal sample library (blue). Counts and curves of all libraries are scaled to fit median counts of normal library 1. Bins were randomly sampled from chromosome 1, and counts include fragments from both strands.

computed for each group the observed 0.1 and 0.9 quantiles. Plotted against the estimated rate of the group, each quantile level forms a curve. The distance between the curves reflects the variation around predicted means. When this distance is considerably larger than that of the Poisson, this indicates that different rates were assigned to the same predicted value, meaning that much variation remains unexplained by the model.

4 Results

4.1 Bin Counts

The GC effect for human genomes is largely unimodal. In AT rich regions, coverage increases with increasing GC. In GC rich regions, coverage decreases with increasing GC. The peak coverage can be different for different data sets (and bin sizes), but is usually located between 0.4 to 0.55 GC. That 10 kb bins with GC > 0.5 are rare in the human genome is perhaps the reason for calling GC effect “linear”. This unimodal relation can be seen at almost any scale, from 50 bp to above 100 kb. While in the AT rich region the increase in coverage is quite linear with GC, it is less linear (and more variable) in GC rich regions.

The curves of difference samples are all unimodal, but not the same: The slopes, location of mode,

and variance around the unimodal curves vary considerably between samples. Indeed, variability between curves was found not only between labs or protocols, but also between tumor and normal sample pairs and between different libraries based on the same starting DNA. In Figure 2 (A), we compare the GC curves of two libraries prepared from the same normal genome. The curves are not aligned: for GC poor bins fragment counts of the library 1 are higher compared to library 2, while in GC rich bins fragment counts of library 2 is lower. Moreover, the GC curve (B) of normal library 1 (blue) does not follow the curve of tumor library 1 (red), displaying both different slopes and different peak locations (B). The curve for the tumor peaks at a GC of 0.55, but for the normal library 1 it peaks at 0.48 (and library 2 at 0.5).² This makes a case for the importance of single sample normalizations (and library specific normalizations). However, different regions in the genome (SM Figure 13) do have similar GC curves. Also, different lanes of the same library (on a single flow cell) display the same curve (not shown).

The choice of bin size should not matter much if the bias is linear. However, sampling a unimodal curve at the wrong scale will normally increase the variance. We therefore compared the absolute deviance from the curve at different bin sizes (Table 2). The predictions were aggregated to 10 kb (regardless of estimation bin size). The results improve as bin size decreases. This is true, for both libraries, until we approach bin sizes of the order of the fragment length (300 bp for library 2, 200 bp for library 1). Counts of library 2 were scaled by median fragment rate to match library 1.

Loess bin size (kb)	10	5	2	1	0.5	0.2
Normal Lib1	49.1	47.8	45.1	43.4	43.4	52.2
Normal Lib2	54.8	52.0	47.5	45.7	49.7	87.7

Table 2: **Prediction error (MAD) of loess model for different resolutions.** Error measured by mean absolute deviation around the predicted rates. Rates were estimated using loess at the specified resolution, and then predictions were aggregated into 10 kb bins.

Indeed, we cannot expect reducing bin sizes to work for such small scales. On scales comparable to fragment sizes the bin-edge effects become substantial. Each of the different models for the GC effect (fragmentation, reads, or full fragments) should imply a different correction strategy. Moreover, small bins have few reads / fragments, and so measuring variability around the mean becomes harder. Instead of binning, single position models (see Figure 1) are introduced to measure GC effects in these smaller scales.

4.2 Single position models

Single position models allow us to compare different possible GC windows, estimate the effects for each, and compare their TV scores. First we compare TV scores of GC windows starting at the 5' end ($a = 0$) of a location (but having different lengths). We would expect to see the strongest effect either after a few bp (fragmentation effect), after 30-75 bp (read effect) or at the fragment lengths (full-fragment effect).

For both libraries, the full-fragment model achieves the highest TV score. In Figure 3 (A), the two curves represent TV scores of the two libraries from the normal sample. The horizontal bars on the bottom mark the median (and 0.05, 0.95 quantile) fragment sizes for the two libraries.

²That tumor has only a single band reflects that there were no large copy-number events in chromosome 1; this is not true in general, see for example Figure 9

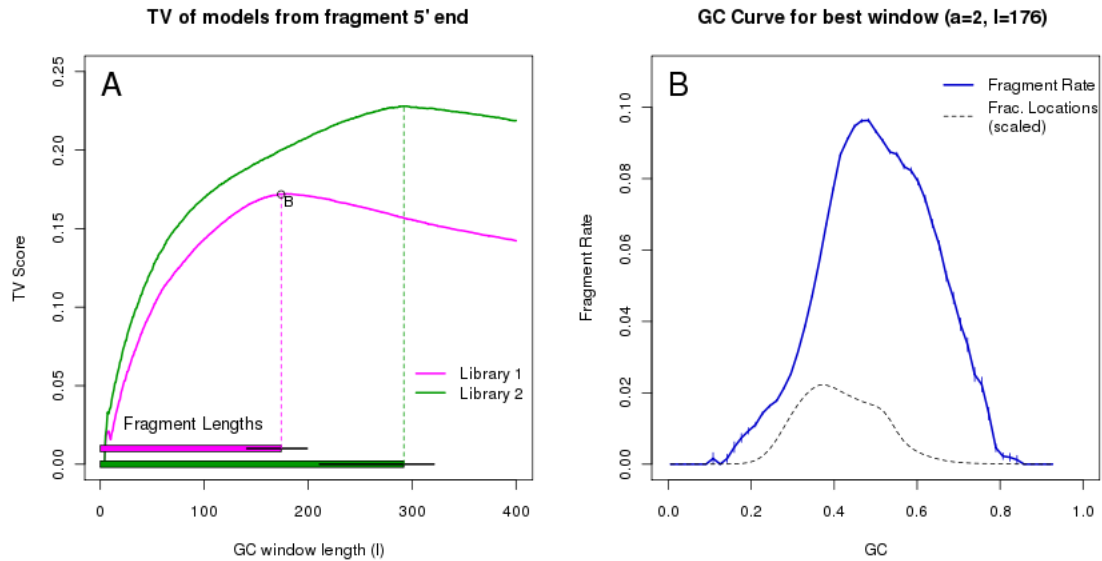


Figure 3: **Single position models.** (A) The top curves represent TV scores for GC windows of different lengths, all beginning at 0 ($a=0$). The bars on the bottom mark the median fragment lengths (and 0.05, 0.95 quantiles). For each library, the strongest GC windows are those that encompass the full fragment. For library 1, we mark the optimal model ($W_{0,180}$), and show its resulting GC curve on the left panel (B). (We actually show $W_{2,176}$, removing 2 bp from each side of the fragment). The GC curve measures the fragment rate given the fraction of GC in the window. Vertical bars represent 1 std-dev. For comparison we plot the distribution of GC (dotted line) in our sample from chromosome 1 (scaled).

TV-scores for both libraries increase as the window size increases, with the strongest effects for windows almost matching the median fragment length: strongest effect for window of length 180 ($W_{0,180}$) for library 1 (median length = 174), and length 295 ($W_{0,295}$) for library 2 (median length 293). For windows longer than that, the scores decrease.

The GC-curve that is estimated from the window $W_{2,176}$ is extremely sharp, see Figure 3 (this is $W_{0,180}$ after removing 2 bp on each end). In fact, strong unimodality can be seen on even smaller scales. Smaller windows ($l = 50$ bp) allow us to contrast a GC window that overlaps the read with a GC window that does not ($W_{0,50}$ vs $W_{75,50}$). (Figure 4, B and C). The GC-effect estimated from both windows has a unimodal shape, but the curve of the window overlapping the read is not as sharp as that of the window from the fragment center. If read-composition were driving the GC-effect we would expect the first window to generate the sharper curve. That this is not the case, may imply that the GC effect is not driven by base calling or sequencing effects, but by the composition of the full fragment. (Rather, the sharper curves in the center imply a second weak bias near fragment ends, see below). For contrast, panel A shows the GC curve estimated from the 50 bp located just outside the fragment ($W_{-50,50}$). The curve is not unimodal, and has a noticeably lower TV score.

To further illuminate this (Panel D), we compute TV scores for other 50 base-pair GC windows with different lags. The TV curve traces the shape of the fragments: It ascends sharply for windows completely within the fragment, and then dips considerably for windows outside the 3'

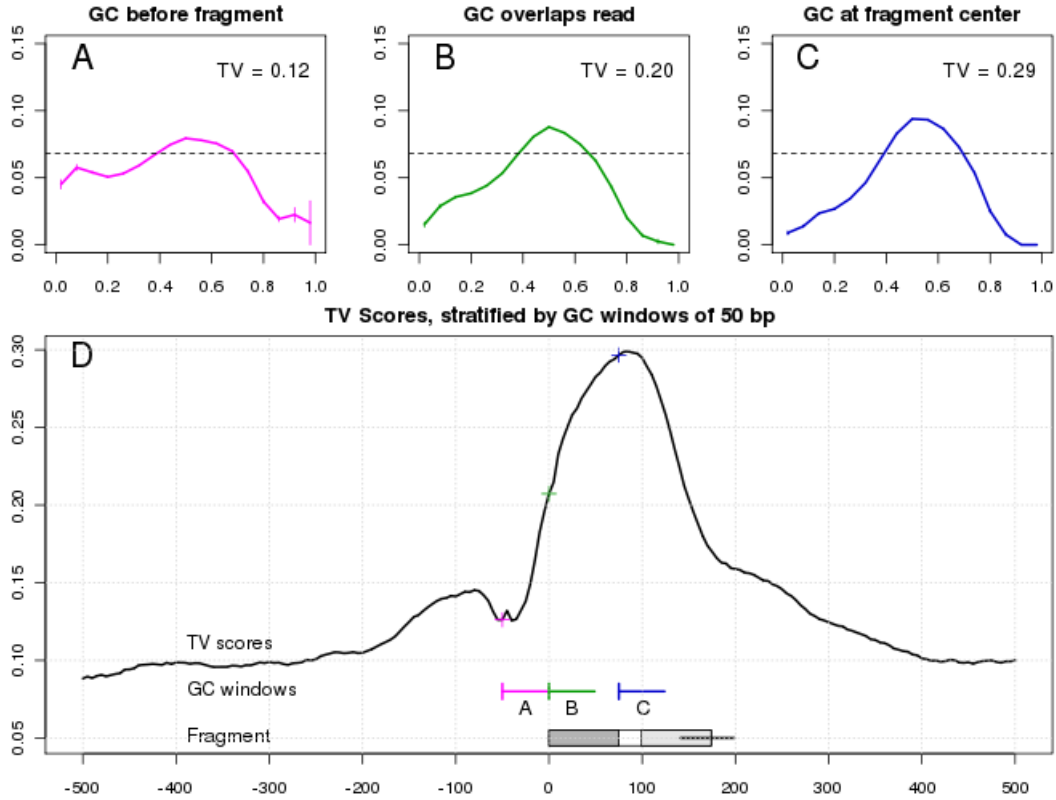


Figure 4: **Different lags** (A) GC curve of the window before the fragment - $W_{-50,50}$, (B) within the read - $W_{0,50}$, and (C) in the fragment center, not overlapping the read - $W_{75,50}$. (D) A plot of TV scores for 50 bp sliding windows. The x-axis marks a , the location of the window 5' end relative to 5' end of the fragment. On the bottom we mark a fragment and its reads in relation to the GC windows from the top panels.

end. The line is mostly symmetric around half the median-fragment length, decreasing as the windows extend over the 3' ends of fragments. In fact, enumerating over many positions a and lengths l , the strongest windows are those overlapping most of the fragment but excluding the fragment ends. (Note that the 5' end is perfectly aligned, the 3' is not, due to varying fragment lengths).

In Supp. Figure 14 we contrast the TV plots generated from the forward strand with TV plots of the reverse strand. While the reads have exactly the same location (no matter the strand), the forward strand fragments extend to the 3' end of the read while reverse strand fragments extend to the 5' end. The TV score lines trace these shapes. After the proper inversion and shift, both GC curves estimated on the reverse strand and their TV scores match those from the forward strand.

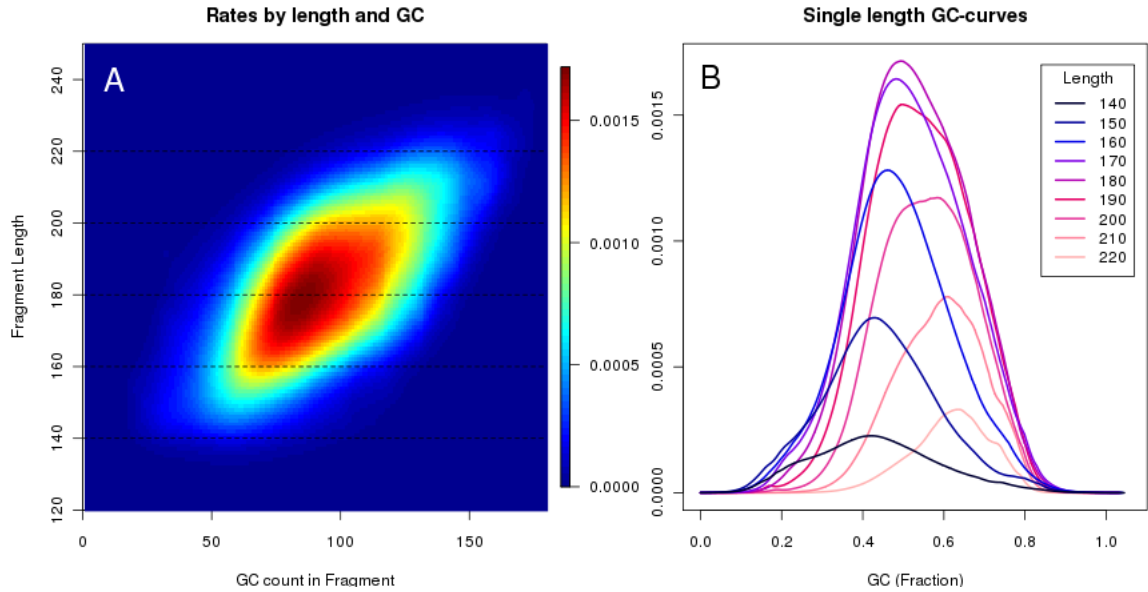


Figure 5: **Fragment rate by length and GC.** (A) A heat map describes rates for each (GC, length) pair. Each dotted line represents a single length. In (B), GC curves for fragments of specific lengths are drawn (corresponding to the dotted lines in (A)). Blue / dark curves represent longer fragments than red / bright. Here x-axis is the fraction of GC. All fragment length models here have a margin of 2 from both fragment ends ($a = 2$, $m = 2$).

4.3 Effect of fragment length

Within a library, we find that the length of fragments influences the shape of the GC curve. If GC depends on fragments and not reads, the GC is a quotient of two fragment parameters: the number of G and C bases, and the length of the fragment. We might expect the two parameters to interact to determine the rate of fragments. This is indeed the case. Within a single library, GC curves estimated on longer fragments peak at higher GC's.

Figure 5 (A) displays a surface describing fragment rates for all (GC, length) pairs. We use the GC count of the full fragment excluding the first 2 bp on each end, corresponding to $W_{2,s-4}^s$. Each horizontal cut of this surface represents a GC curve for fragments of a specific length.

Models restricted to long fragments (top) tend to reach highest rates at higher GC counts (right). The shift toward high GC in longer curves persists in the rescaled curves (B). The curves displayed here are represented by the dotted lines on (A), rescaled so that the x-axis is the fraction GC, not the count. We have seen similar patterns of GC-length interactions in other data sets from different sequencing centers, though not all.

4.4 Local biases near fragment ends

While the unimodal effect is the strongest inhomogeneity in coverage, it is not the only one. We will discuss two (perhaps partially related) effects that are found near the fragment ends, and argue they are not driving the GC effects at larger bin sizes.

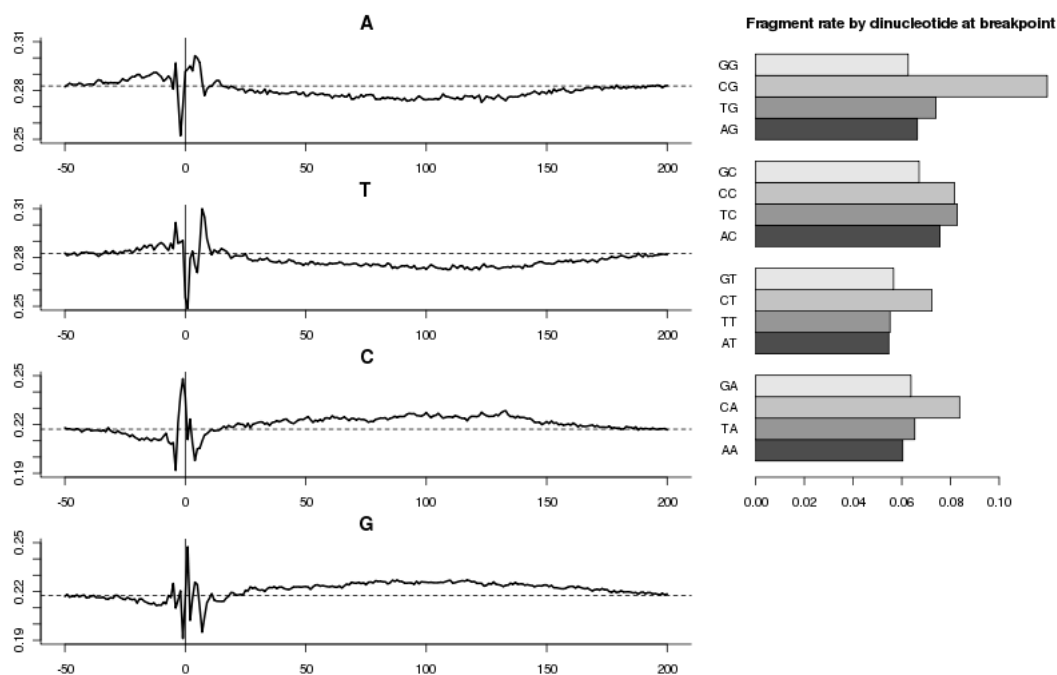


Figure 6: **Fragmentation effect.** Left: Relative abundance of nucleotides at fixed positions relative to fragment 5' end. A horizontal dotted line marks the relative abundance of the base at mappable positions. Right: Fragment rates when stratifying by the dinucleotide (-1,0). Dinucleotide counts overlapping the fragment 5' end.

The first of these is a preference of AT near the fragment ends. Note that the GC curve based on a window just 5' to the fragment (Figure 4, panel A) reveals a second mode of AT rich windows (in addition to the mode at 0.5 GC). Traces of this mode can also be seen in Panel B overlapping the read. The TV score when stratifying by this window are indeed lower (compared to the center of the fragment), reflecting the conflicting effects. This phenomena is strongest for 20-30 bp surrounding both the 5' and 3' end.

A second bias is in the composition of the few bp around the fragment ends. It has been described before in RNA-seq [8]. The relative frequency of nucleotides follows a position-specific pattern roughly starting 4 bases before fragment and ending 8-9 bases inside it (see Figure 6, Left). We call this the *fragmentation effect*. Note that G and C are differently preferred, and so is A compared to T. Complementary effects can be seen on the 3' end of the fragment, for a fixed fragment size. The fragment-GC effect described before can also be seen - the small preference of G and C between 20 and 200 (reflecting fragment sizes). Rates stratified by dinucleotide counts are significantly different than singletons. In particular, the dinucleotide on which fragment rates depend the most is the pair surrounding the fragment end (the breakpoint), shown on the right. Fragments are much more likely to start within a CpG dinucleotide, than any other dinucleotide.

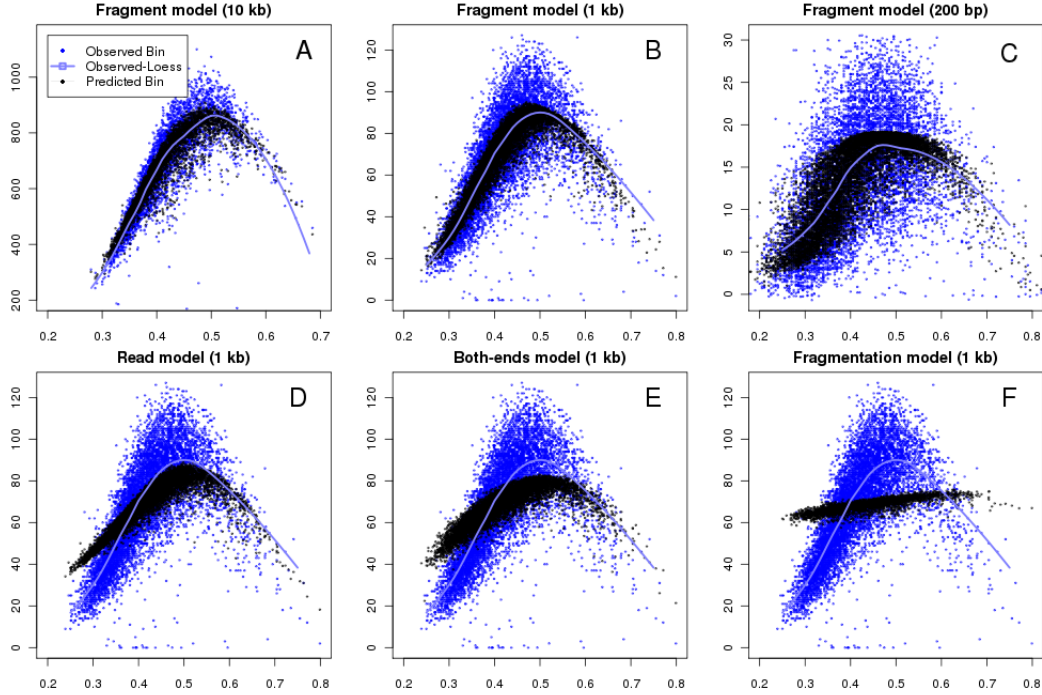


Figure 7: **Aggregation of single location estimates.** (A-C) Estimates based on the fragment GC curve (black) trace similar paths as loess (cyan) estimated on observed counts (blue) on multiple scales. (D-F) Estimates based on alternative models compared to observed counts on 1 kb bins. (D) *Read model*, predictions based on GC of the 5' read only ($W_{0,75}$); (E) *Two-ended model* uses GC (30 bp) from both ends of the fragments; (F) *Fragmentation model* based on location specific composition around the 5' end. See Supp A.1 for details on how models for (E) and (F) were defined and estimated.

4.5 Aggregating effects and corrections

Local effects captured by the fragment model drive the GC curves found at larger scales. In Figure 7, Panels (A)-(C) compare GC to predicted and observed bin counts at various bin sizes. For all three bin-sizes, the predicted counts (black) trace the observed loess line (blue), but also capture some of the variability around the curve.

In contrast, models based on smaller portion of the fragment do not trace the observed curves. Panel D shows the estimates from the read ($W_{0,75}$). The predictions are too high for GC rich or GC poor bins, and too low for intermediate GC bins. Similarly, the *two end model* (E), using GC (30 bp) from both ends of the fragment, produces unimodal predictions which are not sharp enough to capture the observed shape. Prediction based on the *fragmentation model* (F) does not produce sharp contrasts or unimodality. The methods of correction used for (E) and (F) are described in detail in A.1.

Correction based on the fragment and fragment-length models remove most GC dependent fragment count variation. Predicted counts based on the fragment model are more accurate than predictions from the optimal loess model (MAD = 9.5 for fragment model, compared to 10.8 for loess model on 1 kb bins). The same holds for all bin-sizes. Adding fragment-length into this

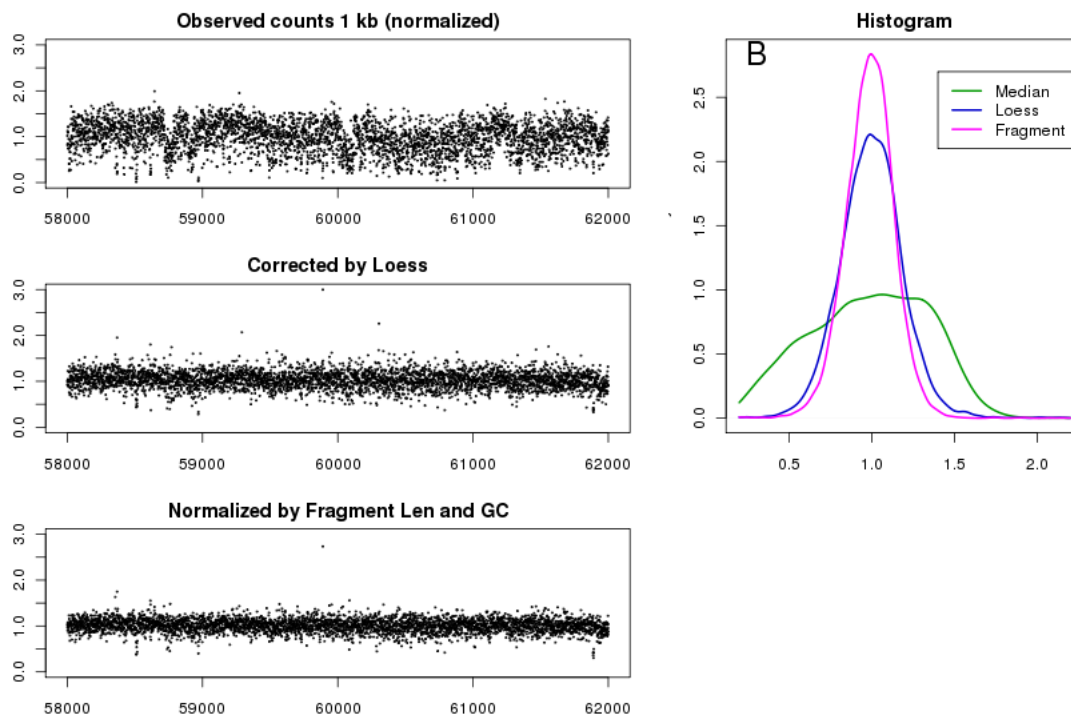


Figure 8: **Corrected counts of normal sample.** (A) Counts in 1 kb bins not corrected for GC (top), corrected by loess (center), and corrected by fragment model (bottom), positions 7,000-12,000 kb of chromosome 1. (B) Histograms of the corrected counts (random sample of 1 kb bins). Each point represents counts from both libraries (forward strand).

model does not considerably change the prediction quality ($MAD=9.1$). Because adding length did not improve the results considerably, we use the parsimonious fragment model for the rest of this work.

We visualize the correction in a region of chromosome 1 which has no copy number (CN) changes (Figure 8). On the left, uncorrected (but scaled) 1 kb bin counts display large low-frequency variations, which can be mistaken for CN events. The fragment model removes these variations better than the loess model. In (B), a histogram of corrected counts shows that the fragment correction produces tighter distribution of counts around 1 compared to the loess model.

A similar correction on the tumor data reveals a hidden CN (both libraries, forward strand) in Figure 9. GC-curves (for both the loess and fragment models) were estimated from chromosome 1, and corrected counts for a CN gain on chromosome 2 are shown. The CN gain is hidden in the uncorrected data due to low-frequency count variation driven by GC-content. Both the fragment model correction and the loess correction reveal the CN gain. The fragment correction provides better separation between bands (see histograms in (B)). Also, it successfully corrects for different binning resolutions (see Supp Figure 15). Note that chromosome 1 was used for GC estimation because it does not seem to have large CN changes (as seen in Figure 2).

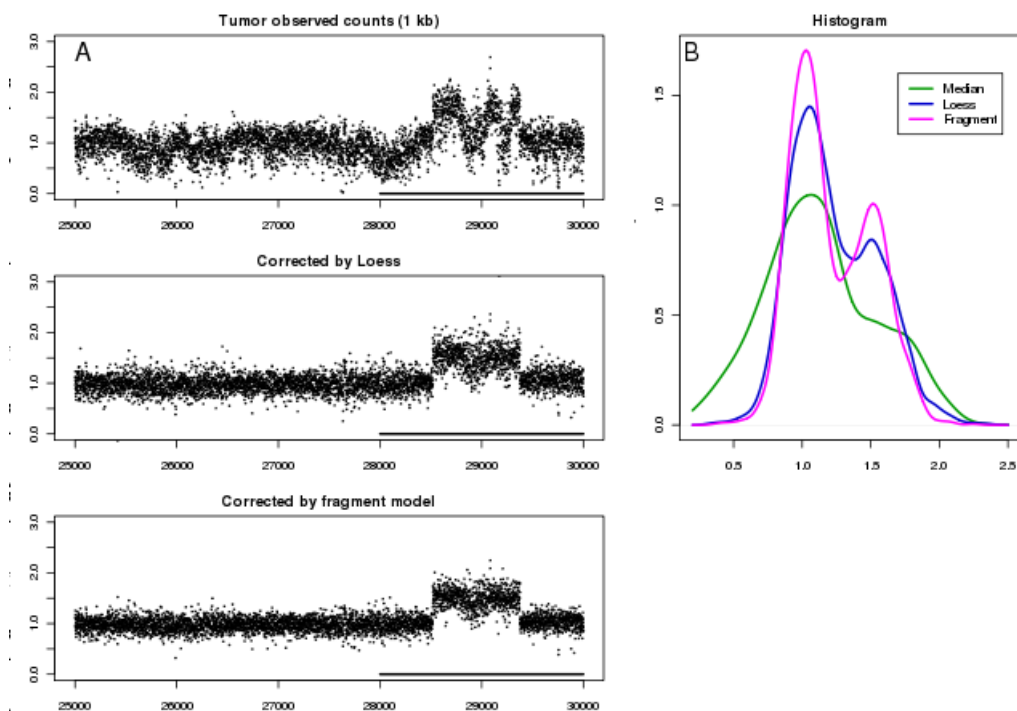


Figure 9: **Copy number (CN) gain from tumor sample** Counts and corrected counts at position 29,000 kb on chromosome 2. (A) Unnormalized counts at 1 kb bins (top), corrected by loess (center), and corrected by fragment model (bottom). GC curves estimated on chromosome 1 (which has no large CN changes). (B) Histogram of normalized counts at 28-30 mb (underlined on left plots).

4.6 Poisson and other variation

The estimated GC-effect and mappability explain most the variation in the fragment coverage of the normal genome (though not all of it). In Table 3 we compute the residual variance after removing the GC-effect in 1 kb bins. The GC model removes most of the variability in the binned counts, much more so than corrections based only on mappability. The residual variance of the fragment models is considerably smaller than that of the loess model. It is still larger than Poisson, though small areas with extremely high coverage cause most of this extra variance.

For a comparison more robust to these high-coverage regions, we compare quantiles rather than variances. In Figure 10, we compare the 0.1 and 0.9 quantiles of observed counts grouped by the estimated fragment rates of different models (see Methods). The variation in bins with very low observed counts is largely explained by mappability. However, mappability cannot explain variation of higher counts, and the spread between the quantiles is approximately double that of the Poisson. Models taking GC-content into account produce much tighter spreads. The fragment-length model (the green curve) consistently leaves less variation around the estimated rates than the loess model (blue).

GC method	Total	Map Residual (MR)	GC Residual (GR)	MR Explained 1-GR/MR	Poisson	GR/Poisson
Loess	909	464	177	0.61	59	3
Fragment	909	464	137	0.7	59	2.33

Table 3: **Residual variance from models.** Residual variance of GC models (GC Residuals), compared to residual from mappability model and to the expected variance of a Poisson. MR Explained refers to the proportion of residual variance (after mappability correction) explained by GC. Computed on 1 kb bins from normal sample (forward strand, library 1), after removing outlier bins.

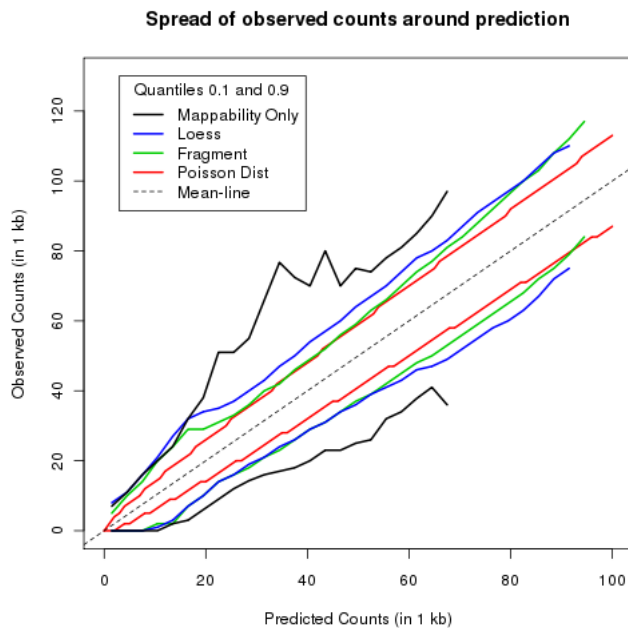


Figure 10: **Comparison to Poisson variation.** 0.1 and 0.9 quantiles of observed counts grouped by estimated rates. Models that predict better will have narrower vertical spreads. Variation around the mean of the fragment-length model (green), the loess (blue) and mappability (black) are compared to variation around a Poisson (red).

4.7 Quality score of mapped reads

Quality scores from the sequencing step can help us assess the role of the sequencing itself (rather than the library preparation) in creating the GC bias. We cannot tell these two stages apart by comparing the sequenced fragments to the reference genome. However, if there are no biases beyond the library preparation, sequencing quality should not reflect any biases in GC. We use the *mapping quality score* [14] of a fragment (actually of the 5' end read), an aggregate of the phred quality scores of the bases in the read that do not match the reference. Scores indicating low quality identify fragments (reads) that probably have sequencing errors ($\Pr\{\text{Mapping error}\} > 10^{-6}$). By comparing the GC profile of low and high quality fragments, we can learn about the relation between GC and sequencing success.

Lower quality scores are strongly associated with GC rich fragments. In Figure 11, we partition the fragments based on their GC, and show the absolute (A) and relative (B) abundance of the two quality groups. Low mapping (black) quality fragments are a much larger portion of high GC fragments, and are very rare in high AT fragments. In fact, almost all high-GC fragments that are mapped are of low quality. This is perhaps an indication of problems with sequencing fragments with very high GC fragments. Surprisingly, this difference in GC composition is stronger for the GC of the full fragments than that of the reads (not shown).

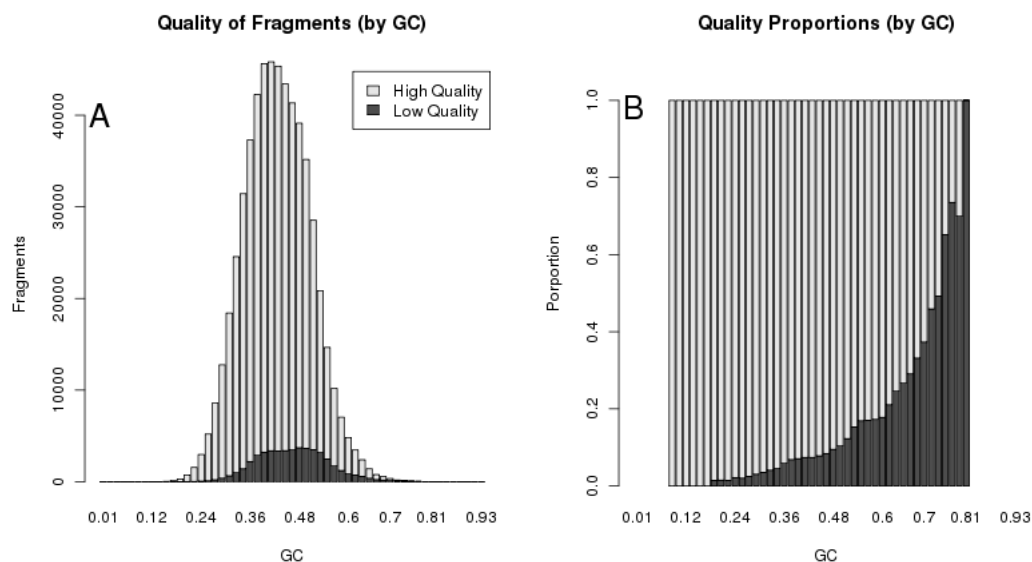


Figure 11: **Fragments partitioned by quality score.** (A) Number of low quality (dark grey) and high quality (light grey) fragments mapping to sampled locations, for each GC category. (B) Proportion of fragments with low vs. high quality for each GC category. GC is determined as in the fragment model with $a = 2, l = 176$. Fragment is high quality if 5' end read has $\Pr\{\text{Mapping error}\} < 10^{-6}$.

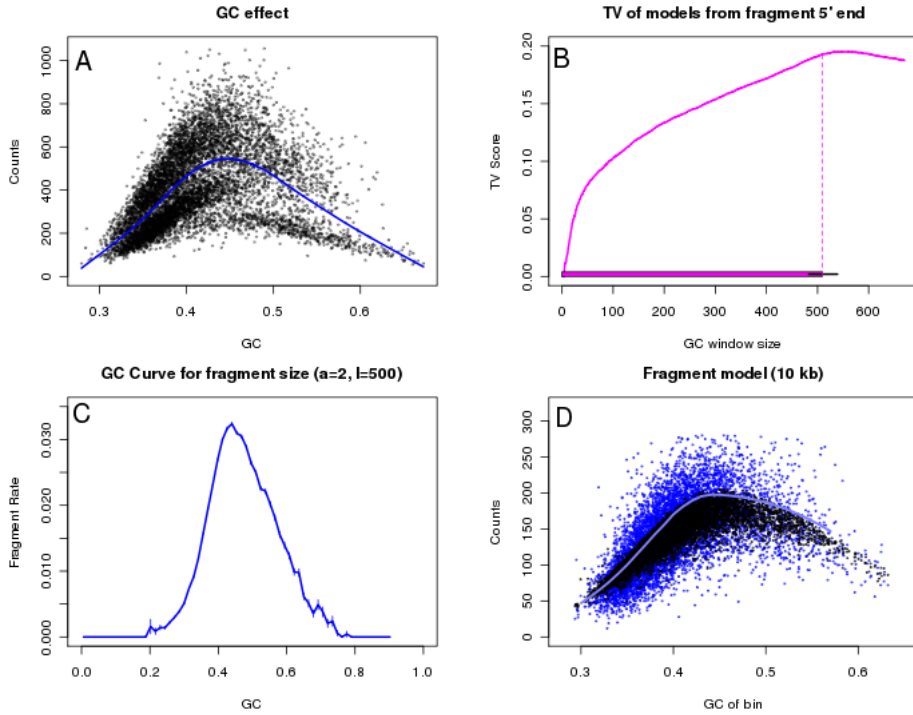


Figure 12: **GC plots for Dataset 2.** (A) GC effect for 10 kb (chromosome 1). (B) TV scores for GC windows of different lengths with $a=0$ (comparable to Figure 3). (C) GC curve at fragment model ($W_{2,500}$). (D) Observed (blue) and predicted (black) counts against GC for 10 kb bins (chromosome 2).

4.8 Additional data sets

In the above analysis we described a single tumor-normal pair produce from a single lab, but our results are general to many examined samples from multiple labs. In Figure 12 we show 4 descriptive plots from a different data set (based on HCC1569 cell line, see Table 1 for details). The GC has a strong effect on fragment counts, and this relation is unimodal (A). The highest TV score is for a window of approximately fragment length (B), resulting in a sharp GC curve (shown in C) which predict the GC trends (D). A distinct difference is the lack of length-dependence of the fragments (not shown). The AT preference near fragment ends is also missing, further evidence that it is not the major source of the GC bias.

5 Discussion

Large biases in fragment counts related to the GC composition of regions were found in the data sets we examined. These observed effects have a recurring unimodal shape, but varied considerably between different samples.

We have shown that this GC effect is mostly driven by the GC composition of the full fragment. Conditioning on the GC of the fragments captures the strongest bias, and removing this effect

provides the best correction, compared to alternative GC windows. Aggregating predictions based on the fragment composition traces the GC curve for larger bins. This cannot be said about local effects that take only the reads into account. This conclusion holds for various data sets, with different fragment-length composition, read lengths, and GC-effect shapes.

That the GC curve is unimodal is key to this analysis. In all data sets shown, the rate of GC poor or GC rich fragments is significantly lower than average, in many cases zero. Unimodality was overlooked by Dohm et al[7], probably because GC-rich areas are rare (especially in simpler organisms). Even in humans, it is hard to spot this effect if counts are binned by GC quantiles instead of GC values. Nevertheless, it is this departure from linearity that allowed pinpointing an *optimal* scale - the fragment size. In that, unimodality gives us important clues as to the causes of the GC bias.

While we have described other sequence-related biases, we believe they are not driving the strong fragment GC-effect. These include an increased coverage when the ends are AT rich, and location-specific fragmentation biases near the fragment ends. We have shown that the end-effects, as measured on the 5' end, are far weaker than the effect from the full fragment. They are surprisingly negligible in the context of larger bins. Still, they might locally mitigate the fragment GC effect: the effect of fragment length on GC curve seems to be associated with these biases.

Our conclusions seem to complement those of Aird et al[1]. If PCR is the major source of the GC bias, we would expect GC of the full fragment to be associated with the bias, rather than the GC of one or both reads. A data-set from the Broad institute, which was generated using the optimized protocol described in [1] [[NOT YET VERIFIED]], does seem to have reduced fragment-wide GC bias (Supp Figure 16). (Interestingly, the fragment-end biases are still present).

Our refined description of the GC effect is of practical value for GC correction. First of all, the non-linearity of the GC effect is a warning sign regarding two-sample correction methods. In the main example we study, the pair of normal and tumor samples do not have the same GC curves. We have seen this in additional data sets as well. Using normal counts to correct tumor counts could sometimes produce GC-related artifacts, which might lead to faulty segmentations. The GC effects of samples should be carefully studied before such corrections are made.

A single sample correction for GC requires a model, and we demonstrate the importance of choosing the best model. Overlapping windows smaller than the fragment fail to remove the bulk of the GC effect. Similarly, using read coverage rather than fragment count hurts the correction. Instead, measuring fragment rate for single bp positions, decouples the GC modeling from the down-stream analysis. Thus it removes the lower threshold on the scale of analysis, providing single bp estimates, which can be later smoothed by the researcher as needed (or binned into uneven bins if needed). An important benefit of DNA-seq over previous technologies is that simply repeating the experiment can increase the resolution of the analysis. Our model assures this increased resolution does not hurt the GC correction.

We describe a straightforward way to calculate the predicted fragment count based on GC and mappability. Mappable genomic positions are stratified according to the GC of a hypothetical fragment. A single fragment-rate is then estimated all positions with the same GC. By comparing TV scores, an optimal *fragment length* can be obtained even for single-end data. The sample we used was somewhat arbitrary: much more data could be used (from all chromosomes), but stable rate estimators can be obtained from far smaller samples.

In this work, we estimated DNA abundance from non-tumor genomes, implicitly assuming that abundance of DNA along the genome is uniform. It is true that copy number variation may occur in non-tumor sequences; these jumps are rare however, and by random sampling we hope to average over any large CN changes. That the windows are small should reduce the dependence between GC and specific positions in the genome. From our experience, estimating GC curves using small windows turned out to be surprisingly robust to copy number changes on tumor data (as displayed above). That said, our main purpose was to further the understanding of the nature of the GC effect; corrections for specific applications may require more sophisticated machinery such as co-estimation of the abundance and the GC effect.

Our prediction accounts for a large portion of the variation, but residual variation is still present. Additional inhomogeneities in fragment rates include unexplained hot spots or zero-counts, as well as milder low and high frequency variation in the counts. The first two categories may be due to errors in the annotation of the genome, or amplification artifacts. The latter point to existence of additional factors that affect fragment rates, which is to be expected. We have discussed additional sequenced-related biases, including fragmentation and AT preference. The tools developed here, primarily the total variance scores, allow analysts to further investigate these effects as needed. Nevertheless, by and large, our model successfully describes the bulk of the low-frequency variability which confounds segmentation to copy number regions.

One effect that we have not deeply explored is the relation between sequencing error probability and the GC effect. There have been reports [16] that specific sequences in reads are more prone for errors, for example a GGC sequence. We have shown evidence that the global GC of the fragment can effect the sequencing error probability. A better model for reads that are harder to sequence would allow better estimation of the fragment GC effect in the GC rich regions, and improve the accuracy of the corrections. Jointly correcting by the GC of the read as well as the GC of the fragment may be a useful approximation for this effect.

Our analysis focused only on DNA-seq data from human subjects, but results from this work can be extended. GC content biases were seen in additional experimental protocols using high throughput sequencing. (See SM, and [5] for similar correction approaches in ChIP-seq data). Some of these protocols focus on highly localized signals on the genome, and could also benefit from strand specific and un-even bin normalization. Moreover, when length of the fragments is constrained (exon-sequencing, RNA seq), a model taking both GC and fragment length into account may prove important. We believe that all these applications can benefit from our refined GC model.

A Supplementary Materials

A.1 Alternative models

The following is a detailed description of the prediction procedures for the two alternative models described in 4.5 and in Figure 7, (E) and (F). The first is the two-ends (paired-reads) model that assumes fragment rate is determined by the GC of both ends of the fragment, but not from the fragment center. The second is the fragmentation model that assumes an aggregation of location specific biases around the fragment ends cause the GC bias.

For both models our goal is to predict μ_x , the mean fragment count for a genomic position x . The predicted mean count for a bin b is the sum of predictions for positions x in that bin,

$\hat{\mu}_b = \sum_{x \in b} \hat{\mu}_x$. As with contiguous GC windows described above, we stratify the positions in the sample according to some function of the sequence surrounding them, and then estimate the fragment rate for each stratum.

A.1.1 Two-ends model

Again, let $GC(x + a, l)$ be the GC count of the l bp starting at $x + a$. Under our two-ends model, the fragment count at x depends on $GC(x, l)$ and $GC(x + s - l, l)$, where s represents the fragment size. For simplicity, we stratify x from our sample by the total GC of both ends

$$gc = GC(x, l) + GC(x + s - l, l).$$

This model requires only $2l + 1$ parameters $\lambda'_0, \dots, \lambda'_{2l}$. For F_{gc} the fragments starting at x 's in the stratum, and N_{gc} the number of sample points,

$$\hat{\lambda}'_{gc} = \frac{F_{gc}}{N_{gc}}.$$

The predicted mean count $\hat{\mu}_x$ for position x based on $\hat{\lambda}'_0 \dots \hat{\lambda}'_{2l}$ is

$$\hat{\mu}_x = \begin{cases} \hat{\lambda}'_{GC(x,l)+GC(x+s-l,l)} & \text{if } x \text{ is uniquely mappable} \\ 0 & \text{otherwise.} \end{cases}$$

To generate Figure 7 (E), we used $s = 180$ the median fragment size, and $l = 30$ ³.

A.1.2 Fragmentation model

For this model we would like to study the effect of the biases surrounding the breakpoint, which are base specific and position specific. We therefore assume the rate at position x is determined by the n -mer overlapping x . For this illustration, we associate fragments starting at x with the heptamer starting 2 bp before the breakpoint and extending 5 bp into the read. The rate of x is associated with one of $16384 = 4^7$ parameters $(\lambda''_{AAAAAAA}, \lambda''_{AAAAAAC}, \dots)$.

Let $Y_i \in \{A, C, G, T\}$ be the base at position i , and let $H_i = (Y_i, \dots, Y_{i+6})$ the heptamer starting at i . We assign position x in our sample to strata $S_{H_{x-2}}$. Again let N_h the number of such positions x in our sample, and F_h the count of fragments beginning in these positions. As before,

$$\hat{\lambda}''_h = \frac{F_h}{N_h}.$$

The predicted mean count $\hat{\mu}_x$ for location x based on $\hat{\lambda}''_{AAAAAAA} \dots \hat{\lambda}''_{TTTTTTT}$ is

$$\hat{\mu}_x = \begin{cases} \hat{\lambda}''_{H_{x-2}} & \text{if } x \text{ is uniquely mappable} \\ 0 & \text{otherwise.} \end{cases}$$

This method might be sensitive to over-fitting due to the large number of parameters. In our case, however, it does not seem to capture the structure of the relation between GC and bin-counts. This holds when conditioning on other n -mers surrounding the 5' end of the fragments.

³Taking $l=75$ would have given a two-read model. However, for our data, this would result in a model almost identical to the fragment length. In the HCC1569 data set, where reads (45 bp each) are much shorter than the median fragment length (507 bp), the 2-read model (i.e. $l = 45$) fails to reproduce the GC curve (data not shown).

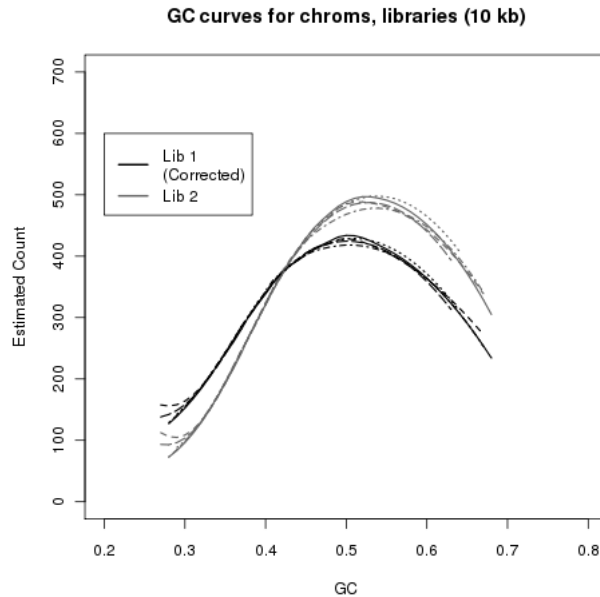


Figure 13: **[[Supp Materials]] GC curves of different chromosomes.** Each GC curve was estimated on data from a single chromosome (chromosomes 1-5, different line types). Different chromosomes display the same curves. Curves of library 1 were scaled (together) to match total fragment count of library 2. Even though libraries are from the same DNA, they display different GC curves. These are from the normal genome of an ovarian cancer patient. In the tumor samples, large differences between curves of different chromosomes may occur due to copy-number events, but their underlying GC shape should be the same.

Bibliography

- [1] D. Aird, M. G Ross, W. S Chen, M. Danielsson, T. Fennell, C. Russ, D. B Jaffe, C. Nusbaum, and A. Gnirke. Analyzing and minimizing PCR amplification bias in Illumina sequencing libraries. *Genome Biology*, 12(2):R18, 2011.
- [2] David R. Bentley, Shankar Balasubramanian, Harold P. Swerdlow, Geoffrey P. Smith, John Milton, Clive G. Brown, Kevin P. Hall, Dirk J. Evers, Colin L. Barnes, Helen R. Bignell, Jonathan M. Boutell, Jason Bryant, Richard J. Carter, R. Keira Cheetham, Anthony J. Cox, Darren J. Ellis, Michael R. Flatbush, Niall A. Gormley, Sean J. Humphray, Leslie J. Irving, Mirian S. Karbelashvili, Scott M. Kirk, Heng Li, Xiaohai Liu, Klaus S. Maisinger, Lisa J. Murray, Bojan Obradovic, Tobias Ost, Michael L. Parkinson, Mark R. Pratt, Isabelle M. J. Rasolonjatovo, Mark T. Reed, Roberto Rigatti, Chiara Rodighiero, Mark T. Ross, Andrea Sabot, Subramanian V. Sankar, Aylwyn Scally, Gary P. Schroth, Mark E. Smith, Vincent P. Smith, Anastassia Spiridou, Peta E. Torrance, Svilen S. Tzonev, Eric H. Vermaas, Klaudia Walter, Xiaolin Wu, Lu Zhang, Mohammed D. Alam, Carole Anastasi, Ify C. Aniebo, David M. D. Bailey, Iain R. Bancarz, Saibal Banerjee, Selena G. Barbour, Primo A. Baybayan, Vincent A. Benoit, Kevin F. Benson, Claire Bevis, Phillip J. Black, Asha Boodhun, Joe S. Brennan, John A. Bridgham, Rob C. Brown, Andrew A. Brown, Dale H. Buermann, Abass A. Bundu, James C. Burrows, Nigel P. Carter, Nestor Castillo,

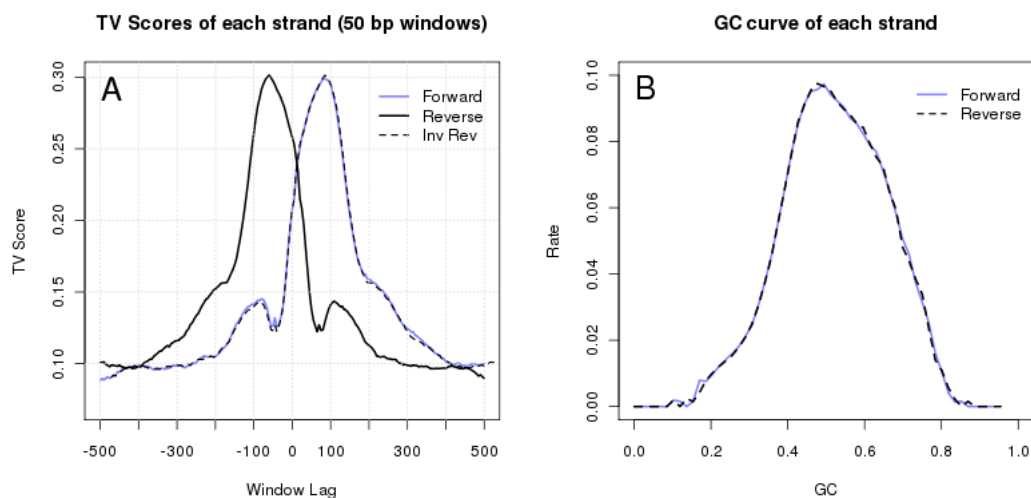


Figure 14: **[[Supp Materials]] GC effect on the strands.** (A) TV Score of 50 bp GC windows, based on forward strand fragments (blue, same as Figure 4, (D)) and reverse strand fragments (black, dot-dash). The dashed line marks the TV scores of the reverse strand after proper inversion (dashed line). (B) Fragment GC curve estimated from each of the strands separately (after accounting for the direction of the fragment)

Maria Chiara E. Catenazzi, Simon Chang, R. Neil Cooley, Natasha R. Crake, Olubunmi O. Dada, Konstantinos D. Diakoumakos, Belen Dominguez-Fernandez, David J. Earnshaw, Ugonna C. Egbujor, David W. Elmore, Sergey S. Etchin, Mark R. Ewan, Milan Fedurco, Louise J. Fraser, Karin V. Fuentes Fajardo, W. Scott Furey, David George, Kimberley J. Gietzen, Colin P. Goddard, George S. Golda, Philip A. Granieri, David E. Green, David L. Gustafson, Nancy F. Hansen, Kevin Harnish, Christian D. Haudenschield, Narinder I. Heyer, Matthew M. Hims, Johnny T. Ho, Adrian M. Horgan, Katya Hoschler, Steve Hurwitz, Denis V. Ivanov, Maria Q. Johnson, Terena James, T. A. Huw Jones, Gyoung-Dong Kang, Tzvetana H. Kerelska, Alan D. Kersey, Irina Khrebtukova, Alex P. Kindwall, Zoya Kingsbury, Paula I. Kokko-Gonzales, Anil Kumar, Marc A. Laurent, Cynthia T. Lawley, Sarah E. Lee, Xavier Lee, Arnold K. Liao, Jennifer A. Loch, Mitch Lok, Shujun Luo, Radhika M. Mammen, John W. Martin, Patrick G. McCauley, Paul McNitt, Parul Mehta, Keith W. Moon, Joe W. Mullens, Taksina Newington, Zemin Ning, Bee Ling Ng, Sonia M. Novo, Michael J. O'Neill, Mark A. Osborne, Andrew Osnowski, Omead Ostadan, Lambros L. Paraschos, Lea Pickering, Andrew C. Pike, Alger C. Pike, D. Chris Pinkard, Daniel P. Pliskin, Joe Podhasky, Victor J. Quijano, Come Raczy, Vicki H. Rae, Stephen R. Rawlings, Ana Chiva Rodriguez, Phyllida M. Roe, John Rogers, Maria C. Rogert Bacigalupo, Nikolai Romanov, Anthony Romieu, Rithy K. Roth, Natalie J. Rourke, Silke T. Ruediger, Eli Rusman, Raquel M. Sanches-Kuiper, Martin R. Schenker, Josefina M. Seoane, Richard J. Shaw, Mitch K. Shiver, Steven W. Short, Ning L. Sizto, Johannes P. Sluis, Melanie A. Smith, Jean Ernest Sohna Sohna, Eric J. Spence, Kim Stevens, Neil Sutton, Lukasz Szajkowski, Carolyn L. Tregidgo, Gerardo Turcatti, Stephanie vandeVondele, Yuli Verhovsky, Selene M. Virk, Suzanne Wakelin, Gregory C. Walcott, Jingwen Wang, Graham J. Worsley, Juying Yan, Ling Yau, Mike Zuerlein, Jane Rogers, James C. Mullikin, Matthew E. Hurles, Nick J. McCooke, John S. West, Frank L. Oaks, Peter L. Lundberg, David Klenerman, Richard

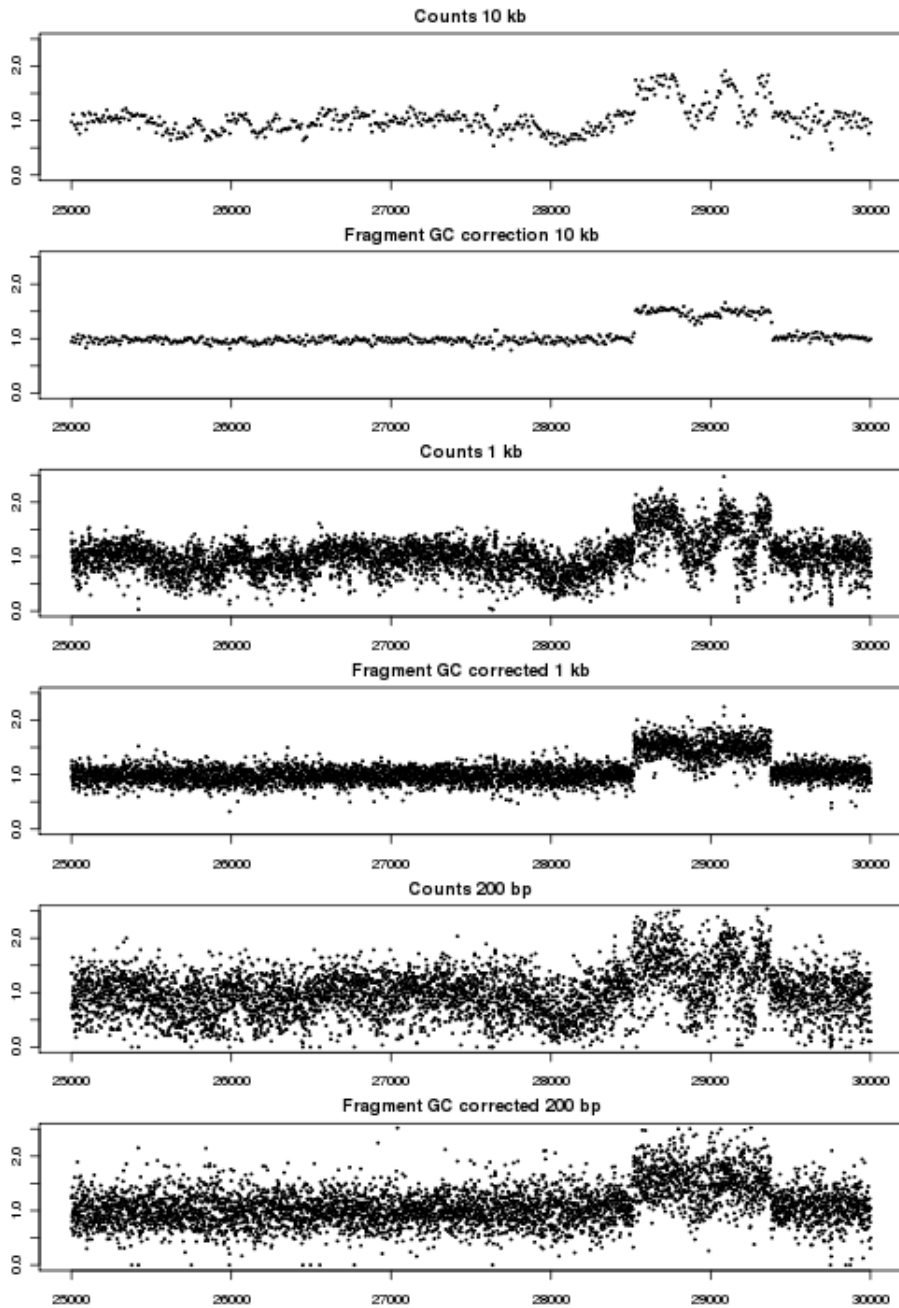


Figure 15: **[[Supp Materials]] Corrections binned at different resolution** A Multi-resolution look at the CN gain shown in Figure 9. The fragment GC model produces a bp level prediction line, which is here binned at 3 resolutions: 10 kb, 1 kb and 200 bp.

Durbin, and Anthony J. Smith. Accurate whole human genome sequencing using reversible terminator chemistry. *Nature*, 456(7218):53–59, November 2008.

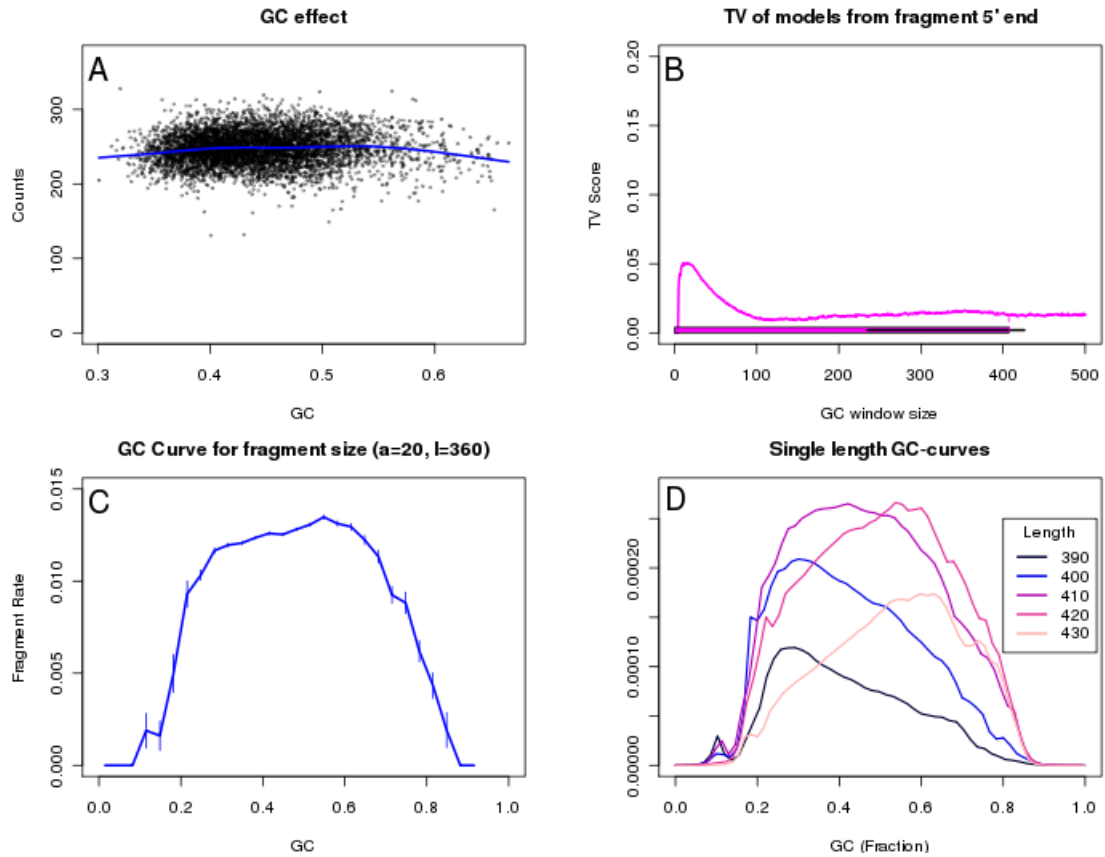


Figure 16: [[Supp Materials]] GC plots for HG00262 sample. (A) GC effect for 10 kb. (B) TV scores for GC windows of different lengths with $a=0$ (comparable to Figure 3). (C) GC curve at fragment model with 20 bp margin ($W_{20,360}$). (D) GC curves for different fragment lengths ($W_{20,s-40}^s$)

- [3] V. Boeva, A. Zinovyev, K. Bleakley, J. P Vert, I. Janoueix-Lerosey, O. Delattre, and E. Barillot. Control-free calling of copy number alterations in deep-sequencing data using GC-content normalization. *Bioinformatics*, 27(2):268, 2011.
- [4] Héctor Corrada Bravo and Rafael A. Irizarry. Model-Based Quality Assessment and Base-Calling for Second-Generation Sequencing Data. *Biometrics*, 66(3):665–674, 2010.
- [5] Ming-Sin Cheung, Thomas A. Down, Isabel Latorre, and Julie Ahringer. Systematic bias in high-throughput sequencing data and its correction by BEADS. *Nucleic Acids Research*, June 2011.
- [6] D. Y Chiang, G. Getz, D. B Jaffe, M. J.T O’Kelly, X. Zhao, S. L Carter, C. Russ, C. Nusbaum, M. Meyerson, and E. S Lander. High-resolution mapping of copy-number alterations with massively parallel sequencing. *Nature methods*, 6(1):99–103, 2008.
- [7] J. C Dohm, C. Lottaz, T. Borodina, and H. Himmelbauer. Substantial biases in ultra-short

- read data sets from high-throughput DNA sequencing. *Nucleic acids research*, 36(16):e105, 2008.
- [8] Kasper D. Hansen, Steven E. Brenner, and Sandrine Dudoit. Biases in Illumina transcriptome sequencing caused by random hexamer priming. *Nucleic Acids Research*, 38(12):e131, July 2010.
- [9] S. Ivakhno, T. Royce, A. J Cox, D. J Evers, R. K Cheetham, and S. Tavaré. CNaseg—a novel framework for identification of copy number changes in cancer from second-generation sequencing data. *Bioinformatics*, 26(24):3051, 2010.
- [10] Pei Fen Kuan; Dongjun Chung; Guangjin Pan; James A. Thomson; Ron Stewart; Sunduz Keles. A statistical framework for the analysis of chip-seq data. *University of Wisconsin, Department of Statistics, Technical Report*, 2009.
- [11] Iwanka Kozarewa, Zemin Ning, Michael A Quail, Mandy J Sanders, Matthew Berriman, and Daniel J Turner. Amplification-free Illumina sequencing-library preparation facilitates improved mapping and assembly of (G+C)-biased genomes. *Nat Meth*, 6(4):291–295, April 2009.
- [12] H. Li and R. Durbin. Fast and accurate short read alignment with Burrows–Wheeler transform. *Bioinformatics*, 25(14):1754, 2009.
- [13] H. Li, B. Handsaker, A. Wysoker, T. Fennell, J. Ruan, N. Homer, G. Marth, G. Abecasis, and R. Durbin. The sequence alignment/map format and SAMtools. *Bioinformatics*, 25(16):2078, 2009.
- [14] Heng Li, Jue Ruan, and Richard Durbin. Mapping short DNA sequencing reads and calling variants using mapping quality scores. *Genome Research*, 18(11):1851–1858, November 2008. PMID: 18714091 PMCID: 2577856.
- [15] Christopher A. Miller, Oliver Hampton, Cristian Coarfa, and Aleksandar Milosavljevic. ReadDepth: A Parallel R Package for Detecting Copy Number Alterations from Short Sequencing Reads. *PLoS ONE*, 6(1):e16327, January 2011.
- [16] Kensuke Nakamura, Taku Oshima, Takuya Morimoto, Shun Ikeda, Hirofumi Yoshikawa, Yuh Shiwa, Shu Ishikawa, Margaret C. Linak, Aki Hirai, Hiroki Takahashi, Md. Altaf-Ul-Amin, Naotake Ogasawara, and Shigehiko Kanaya. Sequence-specific error profile of Illumina sequencers. *Nucleic Acids Research*, May 2011.
- [17] Michael A Quail, Iwanka Kozarewa, Frances Smith, Aylwyn Scally, Philip J Stephens, Richard Durbin, Harold Swerdlow, and Daniel J Turner. A large genome center’s improvements to the Illumina sequencing system. *Nat Meth*, 5(12):1005–1010, December 2008.
- [18] Langmead B; Trapnell C; Pop M; Salzberg SL. Ultrafast and memory-efficient alignment of short dna sequences to the human genome. *Genome Biology*, 10:R25.
- [19] R Development Core Team. *R: A Language and Environment for Statistical Computing*. R Foundation for Statistical Computing, Vienna, Austria, 2010. ISBN 3-900051-07-0.
- [20] Leonid Teytelman, Bilge Özyaydn, Oliver Zill, Philippe Lefrançois, Michael Snyder, Jasper Rine, and Michael B. Eisen. Impact of Chromatin Structures on DNA Processing for Genomic Analyses. *PLoS ONE*, 4(8):e6700, 2009.
- [21] S. Yoon, Z. Xuan, V. Makarov, K. Ye, and J. Sebat. Sensitive and accurate detection of copy number variants using read depth of coverage. *Genome research*, 19(9):1586, 2009.